

Statics and dynamics of domain patterns in hexagonal-orthorhombic ferroelastics

S. H. Curnoe* and A. E. Jacobs†

*Department of Physics, University of Toronto
Toronto, Ontario, CANADA M5S 1A7*

(October 23, 2018)

We study the statics and the dynamics of domain patterns in proper hexagonal-orthorhombic ferroelastics; these patterns are of particular interest because they provide a rare physical realization of disclinations in crystals. Both our static and dynamical theories are based entirely on classical, nonlinear elasticity theory; we use the minimal theory consistent with stability, symmetry and ability to explain qualitatively the observed patterns. After scaling, the only parameters of the static theory are a temperature variable and a stiffness variable. For moderate to large stiffness, our static results show nested stars, unnested stars, fans and other nodes, triangular and trapezoidal regions of trapped hexagonal phase, *etc* observed in electron microscopy of Ta₄N and Mg-Cd alloys, and also in lead orthovanadate (which is trigonal-monoclinic); we even find imperfections in some nodes, like those observed. For small stiffness, we find patterns like those observed in the mineral Mg-cordierite. Our dynamical studies of growth and relaxation show the formation of these static patterns, and also transitory structures such as 12-armed bursts, streamers and striations which are also seen experimentally. The major aspects of the growth-relaxation process are quite unlike those in systems with conventional order parameters, for it is inherently nonlocal; for example, the changes from one snapshot to the next are not predictable by inspection.

PACS numbers: 81.30.Kf, 68.35.-p, 62.20.Dc, 61.70.Ng

I. INTRODUCTION

Ferroelastics^{1,2} are solids that undergo diffusionless, shape-changing phase transformations, usually first-order. The low-temperature (low- T) phase is, in principle, one of several degenerate products (“variants”) differing only in orientation. But one rarely sees the homogeneous product phase; instead, multiple nucleation events, constraints, intrinsic inhomogeneities, *etc*, produce domain structures composed of multiple variants separated by domain walls (ideally with certain orientations³).

This article deals with hexagonal-orthorhombic (H-O) ferroelastics, where the three equivalent stretch directions give rise to three variants. Examples are the mineral Mg-cordierite (Mg₂Al₄Si₅O₁₈, References 2,4–6), Ta₄N (Reference 7), and Mg-Cd alloys (References 8,9). The most interesting feature of these materials is that they provide a rare physical realization of disclinations in crystals^{8,9}. The disclinations result because domain walls rotate the variants as well as link them, all nodes but one failing to close to 360°; the consequence is the fascinating domain patterns observed in these materials and in the closely related trigonal-monoclinic material lead orthovanadate [Pb₃(VO₄)₂, References 10,11]. These patterns differ strikingly from those in cubic-tetragonal (C-T) and tetragonal-orthorhombic (T-O) systems; for example, the star disclination, often self-similarly nested, has no counterpart in the other systems.

Of the several theories^{12–16} dealing with these materials, only that of Wen *et al.*¹⁶ found patterns consistent with some of those observed. Their phase-field kinetic theory is however highly phenomenological, being based

on order parameters with no direct physical interpretation; an expansion to sixth order is necessary, and even the scaled theory requires at least five parameters.

We investigate H-O ferroelastics by expanding the energy density in physical quantities only, namely the strains and their derivatives, to fourth order in the primary order parameter. Computational resources allow us to consider only two-dimensional structures, but this is not much of a restriction, for these are what the literature reports. Our density respects the symmetry of the high- T phase; it is minimal, for it contains only essential terms. Scaling reduces the parameters in the density to two, a temperature variable and a stiffness variable, both readily determined from experiment. Our calculated structures depend strongly on the stiffness, which determines how the system responds to the disclinations generated by wall junctions. We investigate both the statics and the dynamics of the theory, using in both methods which satisfy the compatibility relations exactly.

Our static theory, described in Section II, is based solely on classical elasticity theory; it includes nonlinear and gradient terms but no additional phenomenology. Section III solves for the two kinds of wall linking a given pair of variants. Section IV describes static structures found numerically. Section V first describes the equations of motion of our dynamical theory (also based solely on classical elasticity theory) and then goes on to present structures as they evolve in time.

Although our theory is strictly valid only for proper ferroelastics, where the strain is the primary order parameter, we find that it is sufficient to explain qualitatively the patterns observed in all four materials listed above, namely several kinds of three-fold nodes, a com-

mon four-fold node, stars (both nested and unnested), the fan node and another untitled node, and even imperfections in some higher-order nodes. Near T_c , we find triangular and trapezoidal pockets of the high- T phase, also as observed^{10,11}. Many of these structures were not found by Wen *et al.*¹⁶. Our dynamical studies start from the perturbed high- T phase. In the growth stage, we see 12-armed bursts as observed in Mg-cordierite. In the relaxation stage, but still far from the converged state, we see streamers and striations also as observed, and also the formation of the structures seen in our static studies. These are the first simulations to report the bursts, streamers and striations.

II. STRAINS AND STRAIN ENERGY

Hexagonal-orthorhombic ferroelastics require five strains in general. Since we consider only columnar structures uniform in the 3 direction (normal to the basal plane), we need only the dilatational strain e_1 and the deviatoric/shear strains e_2 and e_3 . In the linear approximation for the strain tensor,

$$e_1 = (u_{1,1} + u_{2,2})/2, \quad (1a)$$

$$e_2 = (u_{1,1} - u_{2,2})/2, \quad (1b)$$

$$e_3 = (u_{1,2} + u_{2,1})/2, \quad (1c)$$

where $\mathbf{u}(x_1, x_2)$ is the displacement of the material point originally at \mathbf{x} , and $u_{i,j} = \partial_j u_i = \partial u_i / \partial x_j$.

The free energy F , per unit length in the 3 direction, is the integral $F = \int_A \mathcal{F} d^2x$ of the free-energy density \mathcal{F} over the undeformed area A . Since the following is the first study of structures in proper H-O ferroelastics, and since there is no evidence that other terms are required, we use the simplest possible density consistent with symmetry, stability and ability to explain qualitatively the structures observed. Of course the terms omitted may be numerically important; in fact a class of these terms is qualitatively important, for we show below that it breaks an important degeneracy.

The minimal density is slightly simplified from one used previously¹³:

$$\begin{aligned} \mathcal{F} = & \frac{A_1}{2} e_1^2 + \frac{A_2}{2} (e_2^2 + e_3^2) - \frac{B_2}{3} (e_2^3 - 3e_2 e_3^2) \\ & + \frac{C_2}{4} (e_2^2 + e_3^2)^2 + \frac{d_2}{2} \left[(\vec{\nabla} e_2)^2 + (\vec{\nabla} e_3)^2 \right]. \quad (2) \end{aligned}$$

All coefficients but A_2 are positive and independent of T . The A_1 and A_2 terms are the contributions from homogeneous volume changes and shears respectively, the latter in the high- T phase only; the parameters A_1 and A_2 are related to the Voigt constants by $A_1 = 2(C_{11} + C_{12})$ and $A_2 = 2(C_{11} - C_{12}) = 4C_{66}$. But A_2 softens with decreasing T , as $A_2 = a(T - T_0)$, where T_0 is the stability limit of the H phase and a is a material-dependent constant. The instability due to the vanishing of A_2 is

isotropic. The orientations of the three O variants are selected by the anisotropic B_2 term, as described below. The quartic C_2 term, isotropic, provides stability. Since e_1 is not the primary order parameter, the term $\frac{1}{2} A_1 e_1^2$ is often omitted^{12,14}. We show below however that this term plays a crucial role in determining the morphology; very different structures are found for large vs. small A_1 . The d_2 term, which penalizes spatial inhomogeneities in the primary order parameter, is necessary to give the domain walls an energy and so prevent subdivision into arbitrarily fine variants. A discussion of other possible derivative invariants is given in the Appendix.

The H-O transition occurs at $A_2 = \frac{2}{9} B_2^2 / C_2$; it is first-order. For $A_2 > \frac{1}{4} B_2^2 / C_2$, the energy has only the H minimum, with $e_1 = e_2 = e_3 = 0$; this minimum disappears for $A_2 < 0$. For $A_2 < \frac{1}{4} B_2^2 / C_2$, there are in addition three degenerate O minima with $e_1 = 0$, symmetrically located in the (e_2, e_3) plane:

$$e_2 = e_{20}, \quad e_3 = 0 \quad (3a)$$

$$e_2 = -e_{20}/2, \quad e_3 = -\sqrt{3}e_{20}/2 \quad (3b)$$

$$e_2 = -e_{20}/2, \quad e_3 = +\sqrt{3}e_{20}/2 \quad (3c)$$

where $e_{20} = \left[B_2 + (B_2^2 - 4A_2 C_2)^{1/2} \right] / (2C_2)$; at T_c , $e_{20} = \frac{2}{3} B_2 / C_2$. The three variants are elongated in the $\hat{1}$, $-\frac{1}{2}\hat{1} + \frac{\sqrt{3}}{2}\hat{2}$, and $-\frac{1}{2}\hat{1} - \frac{\sqrt{3}}{2}\hat{2}$ directions respectively.

III. VARIANT-VARIANT WALLS

We seek the solution linking the two variants of Eqs. (3b) and (3c), the results for this pair being simpler than for the others; the analysis is easily extended to treat a band of walls. The key new results are the expressions (7) for e_1 and ω_3 in terms of e_2 and e_3 .

We start from the first-order compatibility relations $u_{i,12} = u_{i,21}$; with the linearized strain tensor, these are

$$\begin{aligned} \partial_2 (e_1 + e_2) &= \partial_1 (e_3 + \omega_3), \\ \partial_1 (e_1 - e_2) &= \partial_2 (e_3 - \omega_3), \end{aligned} \quad (4)$$

where $\omega_3 = (u_{1,2} - u_{2,1})/2$ is the z component of the local rotation ω . Elimination of ω_3 gives the more familiar second-order relation

$$(\partial_1^2 + \partial_2^2) e_1 - (\partial_1^2 - \partial_2^2) e_2 = 2\partial_1 \partial_2 e_3. \quad (5)$$

On applying the boundary conditions

$$e_2(\pm\infty) = -e_{20}/2, \quad e_3(\pm\infty) = \pm\sqrt{3}e_{20}/2, \quad (6a)$$

$$e_1(\pm\infty) = 0, \quad \omega_3(\pm\infty) = \pm\Omega, \quad (6b)$$

and demanding that the strains and ω_3 be functions of the single variable $X = x_1 \cos \beta + x_2 \sin \beta$, one finds easily the two solutions

$$\beta = 0, \quad X = x_1, \quad e_1 = +(e_2 + e_{20}/2), \quad \omega_3 = -e_3 \quad (7a)$$

$$\beta = \pi/2, \quad X = x_2, \quad e_1 = -(e_2 + e_{20}/2), \quad \omega_3 = +e_3 \quad (7b)$$

Then, with the other two pairings, one has a total of six possible wall orientations, at multiples of $\pi/6$ to the hexagonal 100 axis³. These results are independent of the details of the free-energy density; we made only three assumptions: the strains are small, they (and ω_3) are functions of a single variable, and they have the asymptotic values (6).

The two kinds of wall are orthogonal, as already known³. They are obviously different in nature; it is enough that the angles between the stretch axes are different, but we note also that the dilatational strains have opposite sign in the wall region. The walls need not possess the twin property; in Mg-Cd alloys^{8,9}, the “reflection” walls are twin walls but the “rotation” walls are not.

The rotations in Equations (7) are the key to understanding the domain patterns.

For $\beta = 0$, $X = x_1$: the variant at $x_1 \rightarrow +\infty$, with $e_3 > 0$, is rotated negatively ($\omega_3 < 0$, clockwise); the other variant is rotated positively; the angle between the stretch directions is not $\pi/3$ but rather $\pi/3 - \sqrt{3}e_{20}$.

For $\beta = \pi/2$, $X = x_2$: the variant at $x_2 \rightarrow +\infty$, with $e_3 > 0$, is rotated positively (counterclockwise); ... ; the angle between the stretch directions is not $2\pi/3$ but rather $2\pi/3 - \sqrt{3}e_{20}$.

These rotations are well known in the metallurgical literature, where they are obtained from geometrical considerations. In Mg-Cd alloys, the angles between the stretch axes of the linked variants are calculated from the lattice constants to be⁸ 57.5° or 117.4° , in good agreement ($\pm \sim 1^\circ$) with the observations⁸. The leading corrections to Eqs. (7) (due to nonlinear terms in the strain tensor) are easily found: $e_1 = \pm(e_2 + \frac{1}{2}e_{20}) + O(e^3)$ and $\omega_3 = \mp e_3(1 \mp \frac{1}{2}e_{20}) + O(e^3)$.

Our results for H-O walls are in some respects the same as for C-T^{17,18} and T-O^{19,20} systems. In all three systems, a given pair of variants can be linked by one of two possible walls, at $\pi/2$ to each other³. A given wall not only links the two variants, but also rotates them differentially by an amount proportional to the order parameter, as seen for example in Eqs. (7). Collisions of wall bands generate new kinds of walls²⁰, including a strange “wall” between two variants with identical strains but opposite rotations. In both C-T and T-O systems, where the angle between the variant axes is $\pi/2$ minus a correction, the two possible wall structures are identical with respect to the dilatational and shear strains; in fact, they are related by a symmetry operation, and so have the same energy. In H-O systems on the other hand, there is no symmetry operation relating the two possible structures and so they generally have different energies.

To determine the structure of the wall linking the variants of Eqs. (3b) and (3c), we first use Eqs. (7) to eliminate e_1 from Eq. (2) for the density:

$$\mathcal{F}_{wall} = \frac{A_1}{2} \left(e_2 + \frac{e_{20}}{2} \right)^2 + \frac{A_2}{2} (e_2^2 + e_3^2) - \frac{B_2}{3} (e_2^3 - 3e_2e_3^2)$$

$$+ \frac{C_2}{4} (e_2^2 + e_3^2)^2 + \frac{D_2}{2} \left(\frac{de_2}{dX} \right)^2 + \frac{D_3}{2} \left(\frac{de_3}{dX} \right)^2. \quad (8)$$

Here $D_2 = D_3 = d_2$ for the density of Eq. (2), but D_2 becomes $D_2 = d_1 + d_2$ if the d_1 term is included in the density (see the Appendix); then the length scales of e_2 and e_3 for the wall can in principle be different, even though their gradients appear with the same coefficient. Obviously the two kinds of wall ($X = x_1$ and $X = x_2$) have the same energy. This degeneracy is however due to the particular form of Eq. (2); it is broken if we add to \mathcal{F} any invariant odd in e_1 , for example the term^{21–23} $Ee_1(e_2^2 + e_3^2)$. In principle, such terms can give one wall type a much larger energy than the other; if so, then the domain patterns may be quite unlike those in cordierite, Ta₄N, Mg-Cd and lead orthovanadate.

The compatibility relations are satisfied in Eq. (8), and so the Euler-Lagrange equations can be obtained by varying e_2 and e_3 :

$$A_1(e_2 + e_{20}/2) + A_2e_2 - B_2(e_2^2 - e_3^2) + C_2e_2(e_2^2 + e_3^2) = D_2d^2e_2/dX^2, \quad (9a)$$

$$A_2e_3 + 2B_2e_2e_3 + C_2e_3(e_2^2 + e_3^2) = D_3d^2e_3/dX^2, \quad (9b)$$

with the boundary conditions of Eq. (6a); the A_1 term in Eq. (9a) results from the compatibility relations. Another route to Eqs. (9) starts from requiring F , with the density of Eq. (2), to be stationary with respect to the displacement \mathbf{u} ; then the strains are assumed to depend only on x_1 or x_2 and Eqs. (7) are used to eliminate e_1 ; finally, the results are integrated to give Eqs. (9).

Equations identical in appearance to Eqs. (9) were derived and solved in our study¹⁸ of C-T ferroelastics. At $A_2 = -2B_2^2/C_2$, they have an analytical solution¹⁷ with $e_2 = -e_{20}/2$ and so $e_1 = 0$; at any other T , however, the dilatational strain is not zero in the wall region. The analytical solution at $A_2 = -2B_2^2/C_2$, numerical solutions at other T , and numerical and analytical results for the wall energy are given in Ref. 18. These C-T results carry over to H-O systems with only changes in notation; we point out however that they seem to differ significantly from the results of Ref. 14.

IV. STATIC STRUCTURES

To reduce the number of unknown parameters, we transform variables by

$$e_j \rightarrow [2 \times 10^3 B_2 / (3C_2)] e_j, \quad (10a)$$

$$x_i \rightarrow \sqrt{9d_2 C_2 / (2B_2^2)} x_i, \quad (10b)$$

$$\mathcal{F} \rightarrow [8 \times 10^6 B_2^4 / (81C_2^3)] \mathcal{F}. \quad (10c)$$

Because we work with the displacement, the first (strain) scaling assumes small strains (so that the quadratic terms in the strain tensor can be neglected). We also define a dimensionless temperature by $\tau =$

$(T - T_0)/(T_c - T_0)$, and a dimensionless anisotropy parameter by $\zeta = A_1/A_2(T = T_c) = 9A_1C_2/(2B_2^2)$. In terms of the new variables, the density is

$$\mathcal{F} = \frac{\zeta}{2}e_1^2 + \frac{\tau}{2}(e_2^2 + e_3^2) - \frac{b}{3}(e_3^3 - 3e_2e_3^2) + \frac{c}{4}(e_2^2 + e_3^2)^2 + \frac{1}{2}\left[\left(\vec{\nabla}e_2\right)^2 + \left(\vec{\nabla}e_3\right)^2\right], \quad (11)$$

where $b = 3 \times 10^3$ and $c = 2 \times 10^6$; the scaled theory then has only two parameters, τ and ζ . The transition ($T = T_c$) is at $\tau = 1$, the order parameter at T_c is $e_{20} = 10^{-3}$ (an arbitrary value) and the analytical solution¹⁷ is found at $\tau = -9$. To relate τ to the physical temperature T , we require both T_c and T_0 ; the latter can be estimated from the T dependence of the order parameter (for example, the value at T_0 is 3/2 the value at T_c).

Wishing to study wall configurations, we forced walls into the systems by applying periodic boundary conditions to the displacement \mathbf{u} ; this apparently simple requirement is sufficient to generate many metastable states. Free boundary conditions¹³, it seems, cannot generate the complex structures seen in experiment, and fixed boundary conditions (specifically $\mathbf{u} = 0$ on and outside the boundary^{22,20}) give results which suffer severely from finite-size effects. The static structures described in this section were found by minimizing the free energy with respect to the components of \mathbf{u} , using a conjugate-gradient method; the iteration was continued until numerical errors prevented further decrease in the energy. A variety of starting configurations was used, often random displacements. Finite-size effects are certainly present in the systems we can study (they favour simpler structures); we see the basic structures observed experimentally, however, and so these effects seem unimportant qualitatively.

Detailed comparison with experiment is unfortunately not possible for any of the materials; in fact, experiment offers no guidance at all regarding the parameters τ and ζ of even the minimal theory. Accordingly, we investigated several sets of parameter values; the desired comparison can be made when the parameters are measured.

As the temperature decreases, the order parameter (e_{20}) of the homogeneous (O) product phase increases and the wall width (proportional to $1/e_{20}$) decreases. The two curvatures at the O minima also change, but in different ways. These are γ_{\parallel} and γ_{\perp} in the directions parallel and transverse to the line from the origin to the O minima:

$$\gamma_{\parallel}(T) = \tau - 2be_{20} + 3ce_{20}^2, \quad (12a)$$

$$\gamma_{\perp}(T) = \tau + 2be_{20} + ce_{20}^2; \quad (12b)$$

both increase monotonically with decreasing T . For $T_{BK} < T \leq T_c$ ($-9 < \tau \leq 1$), $\gamma_{\parallel} < \gamma_{\perp}$ with $(\gamma_{\parallel}, \gamma_{\perp}) = (1, 9)$ at $T = T_c$. At $T = T_{BK}$ ($\tau = -9$), the curvature is isotropic, with $\gamma_{\parallel} = \gamma_{\perp} = 27$. For $T < T_{BK}$, $\gamma_{\parallel} > \gamma_{\perp}$. The changing curvatures cause the wall trajectories¹⁸ to start closer to the easy direction in the (e_2, e_3) plane.

The point of introducing these quantities is that our structures depend strongly on the ratio of the curvature ζ (for dilatational strains) to the curvatures $\gamma_{\parallel}, \gamma_{\perp}$ (for departures of the deviatoric/shear strains from values in a homogeneous O variant). This ratio is small for ‘‘soft’’ systems and large for ‘‘stiff’’ ones. This strong dependence on the relative stiffness arises, in the final analysis, because the walls rotate the variants as well as link them. Because of the rotations, disclinations are formed when walls collide to form junctions (or nodes). Since a single disclination cannot exist in a crystal, the walls form arrays of disclinations of both polarities, often in pairs (dipoles) and higher multipoles. Finally, soft systems and stiff systems respond very differently to the disclinations. In soft systems, the walls can deviate considerably from the optimal orientations found above; additional dilatational strains are then generated, but these have low energy since A_1 is relatively small. In stiff systems, on the other hand, the walls are straight on the whole, and their directions are highly constrained; other means must be found to minimize the energy.

To describe the nodes, we use the notation (k, l, \dots) where the components k, l, \dots are successive angles in units of $\pi/6$ (only approximately); this notation, though incomplete because it does not distinguish between the two types of walls, is adequate for our purposes. The 43 possible disclinations, including the star, have been catalogued and the values of the disclination angle δ given for Mg-Cd alloys⁹; those with smallest $|\delta|$ follow⁹:

1. $\delta = 0$ for the (1,3,5,3) node⁷⁻⁹.
2. $|\delta| = 0.243^\circ$ for the star disclination (a three-pointed star with tip angle $\sim \pi/6$, often self-similarly nested), the (1,1,1,1,1,7) fan node, and the untitled (1,1,1,4,1,4) node.
3. $|\delta| = 0.486^\circ$ for the ‘‘starburst’’, our term for a node with 12 walls separated by $\sim \pi/6$.
4. $|\delta| = 2.472^\circ$ or 3.201° for the (1,1,1,1,1,1,1,4) node.
5. $|\delta| = 2.715^\circ$ or 2.958° for the (2,5,5), (1,1,10) and (1,4,7) three-fold nodes and for two five-fold nodes.

Many of the 43 disclinations are not seen because $|\delta|$ is too large; for example, the at-first-thought obvious (4,4,4) node fails by^{8,9} $\sim 8^\circ$. And one expects nodes with many arms to appear less frequently.

Figure 1(a) shows a portion of a structure for a soft system ($\zeta = 10$) at $\tau = -50$, where $(\gamma_{\parallel}, \gamma_{\perp}) \approx (117, 52)$. In this and other structures we found for the same parameter values, we see only three-fold nodes and bends, even though (1,3,5,3), star, fan and other nodes have smaller disclination angles. In such soft systems, the walls can deviate markedly from the high-symmetry directions; they bend gently on the whole, but sharp bends can occur, especially at necks like that at the bottom of the figure. Examination of the rotation ω_3 shows that the necking results from the collision of identical variants with different orientations. As in T-O systems²⁰, the necking reduces the length of the collision region where large dilatational strains are generated. At $\zeta = 1000$, the neck and the $\pi/2$ bends were replaced by a (1,3,5,3) node,

though with other significant changes. Figure 1(a) shows also two well formed (2,5,5) nodes (prominent in Ref. 8); not shown are poorly formed (1,1,10) and (1,4,7) nodes (also seen in Ref. 8). The overall morphology is like that seen in cordierite^{4-6,2}, but lack of detail in the published micrographs prevents a direct comparison; there seems to be room here for further experiment.

Figures 1(b) and 1(c) show typical structures obtained also at $\tau = -50$, but with the moderately soft value $\zeta = 100$. Nested and unnested stars appear, and also (1,3,5,3), (2,5,5), (1,1,10) and (1,4,7) nodes, though all are imperfect. Nested stars like that in part (b) are commonly seen in experiment; the unnested star of part (c) is like that at the right of Figure 3(c) of Ref. 10.

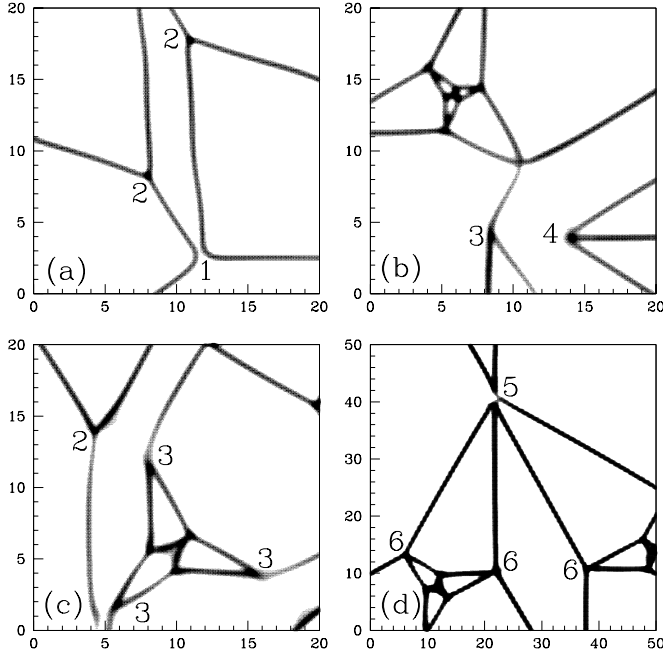


FIG. 1. Greyscale plots of $(e_2^2 + e_3^2)^{1/2}$ for selected regions of static structures. In the white regions, the deviatoric strains are near one of the three orthorhombic minima; the black regions are domain walls. Positions 2, 3, and 4 show (2,5,5), (1,4,7) and (1,1,10) nodes respectively. Part (a) shows a soft system ($\zeta = 10$) at low temperature ($\tau = -50$). The neck at position 1 separates two domains with the same strains but different orientations. Parts (b) and (c), both moderately soft systems ($\zeta = 100$) at $\tau = -50$, show nested and unnested stars respectively. Part (d) shows a moderately soft system ($\zeta = 100$) at a higher temperature ($\tau = -20$); the length scale is different. (1,1,1,4,1,4) and (1,3,5,3) nodes appear at positions 5 and 6.

Figure 1(d) shows a (1,1,1,4,1,4) node, though the vertex is imperfect. This node, similarly imperfect (walls jog at the node), appears in Fig. 7(c) of Ref. 7 and in Figs. 3(b) and 3(c) of Ref. 10. We find that the node tends to split into simpler nodes at lower T , as the effective stiffness ζ/γ decreases. We often observed, but do not display, staircase structures and the “spiral branch

configuration” shown in Fig. 3(a) of Ref. 10.

The structure of Figure 2(a), for a stiff system ($\zeta = 1000$) at $\tau = -50$, shows mostly objects with small disclination angles, namely (1,3,5,3) nodes and stars; the few three-fold nodes are badly distorted (1,4,7) nodes.

Figure 2(b) shows a structure formed close to T_c . The most important features are the triangular and trapezoidal pockets of the high- T (hexagonal) phase; the first is seen in Refs. 10,11, and the second in Fig. 1(e) of Ref. 11. Trapped high- T phase was not seen by Wen *et al.*¹⁶ who looked at a single temperature, perhaps too low. The pockets can be viewed as small grains trapped by rigid walls which prevent them from changing shape; they can transform to the low- T phase only through formation of internal walls, which however cost too much energy at this T . The structure of Figure 2(b) was generated by warming. In the initial structure, the stars were nested and the trapezoids also showed internal structure; both internal structures gradually faded away with warming. Figure 2 of Ref. 11 shows comparable before-and-after pictures found on cooling.

Figure 2(b) shows also the fan node, though the vertex is imperfect. Imperfect fan nodes are seen in Fig. 7(b) of Ref. 7, in Fig. 11(b) of Ref. 8 (the high-resolution image shows 3 three-fold junctions), and in Fig. 3(d) of Ref. 10.

We found structures also for $\zeta = 0.5, 5$ and 50 , at $\tau = 0$, where $(\gamma_{\parallel}, \gamma_{\perp}) = (4.5, 13.5)$; the patterns differed significantly in some respects from those described above. These results and those for $\tau = -50$ suggest that the stiffness ratio ζ/γ is of order 1 for Mg-Cd at the temperature of the observations.

Since ζ/γ depends on T , significant structural changes may result from changing T : if ζ/γ is large at T_c and small at low T , then stars and other structures characteristic of stiff materials may decay as T decreases.

V. DYNAMICS

We derive the equations of motion using the Lagrangian formulation, starting from $\mathcal{L} = \mathcal{T} - \mathcal{F}$ where $\mathcal{T} = \rho(\dot{u}_i)^2/2$ is the kinetic-energy density^{24,13}. The result is

$$\rho\ddot{u}_i = \sigma_{ij,j} + \sigma'_{ij,j} \quad (13)$$

where $\sigma_{ij} = \partial\mathcal{L}/\partial u_{i,j}$ is the stress tensor and σ'_{ij} is the dissipative stress tensor. The most general form for the latter, which describes non-conservative forces (friction) in the system, is $\sigma'_{ij} = A'_{ijkl}\dot{u}_{k,l}$ to lowest order; we note that the dissipation cannot depend on the velocity field \dot{u}_k itself, only on its space derivatives. The dissipative stress tensor is conveniently found from the dissipative function Ψ by $\sigma'_{ij} = \partial\Psi/\partial\dot{u}_{i,j}$. The form which respects the symmetry of the parent (hexagonal) phase is

$$\Psi = \frac{A'_1}{2}\dot{e}_1^2 + \frac{A'_2}{2}(\dot{e}_2^2 + \dot{e}_3^2). \quad (14)$$

We assume that the dissipation is large and drop the inertial term $\rho\ddot{u}_i$; the equations of motion are then

$$\begin{aligned} A'_1\dot{e}_{1,1} + A'_2(\dot{e}_{2,1} + \dot{e}_{3,2}) &= -(G_{1,1} + G_{2,1} + G_{3,2}), \\ A'_1\dot{e}_{1,2} - A'_2(\dot{e}_{2,2} - \dot{e}_{3,1}) &= -(G_{1,2} - G_{2,2} + G_{3,1}), \end{aligned} \quad (15)$$

where $G_i = \delta F/\delta e_i$:

$$G_1 = A_1 e_1, \quad (16)$$

$$G_2 = A_2 e_2 - B_2(e_2^2 - e_3^2) + C_2 e_2(e_2^2 + e_3^2) - d_2 \nabla^2 e_2, \quad (17)$$

$$G_3 = A_2 e_3 + 2B_2 e_2 e_3 + C_2 e_3(e_2^2 + e_3^2) - d_2 \nabla^2 e_3. \quad (18)$$

Actually, we have to use the equations of motion in terms of the displacement components:

$$\begin{aligned} &\begin{pmatrix} A'_1\partial_1^2 + A'_2(\partial_1^2 + \partial_2^2) & A'_1\partial_1\partial_2 \\ A'_1\partial_1\partial_2 & A'_1\partial_2^2 + A'_2(\partial_1^2 + \partial_2^2) \end{pmatrix} \begin{pmatrix} \dot{u}_1 \\ \dot{u}_2 \end{pmatrix} \\ &= -2 \begin{pmatrix} G_{1,1} + G_{2,1} + G_{3,2} \\ G_{1,2} - G_{2,2} + G_{3,1} \end{pmatrix} \end{aligned} \quad (19)$$

The time is scaled so that $A'_2 = 1$; the dependence on the parameter A'_1 was found to be weak during the H-O transition, but the final states (completely relaxed configurations) did depend on A'_1 . We used $A'_1 = 0$ for the results shown in Figure 3.

These equations must be solved numerically. Each time step started with the displacement $\mathbf{u}(x_1, x_2)$ known at the points of a 256^2 grid. The space derivatives of u_i were approximated by finite-difference expressions centered on a 5×5 grid. The non-linear terms on the right-hand sides were computed, and then the equations were fast-Fourier transformed to give algebraic equations. The solutions were advanced in time using the Euler method, and then fast-Fourier transformed back to position space, to start the next step.

All our dynamical studies were started by perturbing the high-temperature state at a single point. The initial state certainly does not represent the nucleus of the transformation, but we expect its growth to resemble that in experiment; in partial confirmation, we see structures much like those observed. The perturbation grows quickly with time, but eventually it collides with self-images generated by the boundary conditions; of course the collision stage also has no relation to experiment. The hexagonal (high- T) phase then disappears (unless the temperature is close to T_c); thereafter, we expect our simulations once again to resemble experiment (again we see structures much like those observed). The relaxation stage which follows is quite slow. We observe the formation of the objects already seen in the static studies reported above, but more interestingly also well-defined structures (streamers, striations) seen infrequently or not at all statically, most of which eventually decay.

In stiff systems (large ζ/γ), large domains can be penetrated by streamers (thin, wedge-shaped intrusions with relatively thick walls off the optimal directions); one often sees also striated patterns of two alternating variants.

The striations and streamers are relics of the H-O transformation. Dilatational stresses occurring at the interface between the high- T and low- T phase are relieved by local fine-scale twinning of the low- T phase²⁵. The result is more complicated domain patterns (striations and streamers) shortly after the transformation is complete. Star embryos appear in the vicinity of triple junctions; these form near mis-oriented or curved domain walls after the surrounding area has transformed. In contrast, systems with small ζ/γ need not reduce dilatational stresses so strongly, and so show no interesting microstructure.

The key difference between the dynamics of ferroelastics and the dynamics of conventional systems is that the former is nonlocal. For example, the retraction of a streamer (or the vanishing of a domain) cannot be effected by local changes; instead, a global change in the displacement field is required. The nonlocality is seen explicitly in theories^{26,27} where effective long-range interactions between the strains are generated on eliminating the displacement. And the relaxation stage is different also in that the changes from one snapshot to the next cannot be predicted by inspection.

Figures 3(a), 3(b) and 3(c) show expanding regions of low- T phase, for stiffness parameter $\zeta = 10, 100$ and 1000 respectively. The 12-arm burst of part (a) is, we suggest, best viewed as a starburst disclination expanding into the high- T phase; it resembles strongly the ‘‘stellate twin’’ of Fig. 1 of Ref. 4 (though the latter is fully developed), consistent with our identification of cordierite as a soft system. The stiffer systems of parts (b) and (c) evolve more slowly; they also show branching at the outer edges, as discussed above.

Figure 3(d) shows the system of 3(b) at a later time. There are several streamers, which retract very slowly with time; similar structures are seen in Fig. 14(b) of Ref. 8. The long timescale associated with this simple evolution (there is no change in the topology of the domain walls) results from the nonlocal relaxation.

Figures 3(e) and 3(f) show the system in 3(c) at a later time. The complicated structures in 3(e) are not observed in softer systems. In stiff systems they are transitory, existing only immediately after completion of the phase transformation. The domain walls near the striations and star embryos are relatively broad and they deviate from their optimal orientations; at later times, for the most part, they are replaced by well-defined walls as shown in the fully relaxed configuration of 3(f). The divided diamond-shaped structure seen at the top of Figure 3(f) is seen in Fig. 9 (especially part (c)) of Ref. 7, suggesting that Ta-N is a stiff system.

VI. SUMMARY

A Landau theory of proper hexagonal-orthorhombic ferroelastics, with the fewest possible number of parameters, describes qualitatively many of the structures

seen in Ta₄N, Mg-Cd alloys and Mg-cordierite, and in trigonal-monoclinic lead orthovanadate. Our static and dynamical studies found structures not previously seen theoretically, including trapped high-temperature phase, 12-armed bursts, streamers and striations.

Since the theoretical understanding of structures in these systems seems now well advanced, we suggest that the next major theoretical task is to include noise and fluctuation effects in the time development. The effect of the inertial term also seems worth investigation.

APPENDIX

Equation (2) contains only one term quadratic in the strain gradients; the most general such expression includes four additional invariants:

$$\begin{aligned} & \frac{1}{2}d_1 \left(\vec{\nabla} e_1 \right)^2 \\ & + d_3 [e_{1,1}(e_{2,1} + e_{3,2}) + e_{1,2}(-e_{2,2} - e_{3,1})] \\ & + d_4 \left[(e_{2,1} - e_{3,2})^2 - (e_{2,2} + e_{3,1})^2 \right] \\ & + d_5 (e_{2,1}e_{3,2} - e_{2,2}e_{3,1}) \end{aligned} \quad (20)$$

The d_1 term may be important more generally, but it can be neglected for the wall structures of interest to us here; it obviously plays no role for stiff systems where $|e_1|$ is small, and we find numerically that it is qualitatively unimportant also in soft systems. Given this, and that we want a minimal theory, we omit the d_3 term also. The d_5 term integrates to a surface term, which vanishes for periodic boundary conditions.

The remaining term (coefficient d_4) is closely related to the d_2 term in Equation (2). To demonstrate this, we consider the sum

$$\begin{aligned} I = & \frac{1}{2}d'_2 [e_{3,1}^2 + (e'_{3,1})^2 + (e''_{3,1})^2] \\ & + \frac{1}{2}d'_4 [e_{3,2}^2 + (e'_{3,2})^2 + (e''_{3,2})^2] \end{aligned} \quad (21)$$

of two non-negative invariants. The primes represent terms obtained by $2\pi/3$ rotations about the hexagonal axis; for example, $e'_{3,1} = \frac{1}{2}(-\partial_1 + \sqrt{3}\partial_2)\frac{1}{2}(\sqrt{3}e_2 - e_3)$. Each of the above six terms corresponds to the change in the order parameter in the direction normal to one of the six different domain-wall orientations discussed in Section III. The explicit expression for I is

$$\begin{aligned} I = & \frac{3}{16}d'_2 [3(e_{3,1}^2 + e_{2,2}^2) + e_{2,1}^2 + e_{3,2}^2 \\ & + 2(e_{2,1}e_{3,2} + e_{2,2}e_{3,1})] \\ & + \frac{3}{16}d'_4 [e_{3,1}^2 + e_{2,2}^2 + 3(e_{2,1}^2 + e_{3,2}^2) \\ & - 2(e_{2,1}e_{3,2} + e_{2,2}e_{3,1})] . \end{aligned} \quad (22)$$

Equivalent results are found on working with e_2 rather than e_3 , for

$$e_{2,i}^2 + (e'_{2,i})^2 + (e''_{2,i})^2 = e_{3,j}^2 + (e'_{3,j})^2 + (e''_{3,j})^2 , \quad (23)$$

with $i \neq j$.

The isotropic case corresponds to $d'_2 = d'_4$; then I equals the d_2 invariant we used in the free energy. The d_4 invariant is found from the difference, $d'_2 = -d'_4$. In keeping with our goal of a minimal theory, we consider the isotropic case and omit the d_4 term in the free energy.

ACKNOWLEDGMENTS

We thank Colin Borys for technical assistance. This research was supported by the Natural Sciences and Engineering Research Council of Canada.

* Electronic address: curnoe@physics.utoronto.ca

† Electronic address: jacobs@physics.utoronto.ca

¹ K. Aizu, J. Phys. Soc. Jpn. **27**, 387 (1969).

² E. K. H. Salje, *Phase Transitions in Ferroelastic and Coelastic Crystals* (Cambridge University Press, Cambridge, 1993).

³ J. Sapriel, Phys. Rev. B **12**, 5128 (1975).

⁴ V. Venkatesh, Am. Mineral. **39**, 636 (1954).

⁵ A. Putnis, E. Salje, S. A. T. Redfern, C. A. Fyfe and H. Stobl, Phys. Chem. Minerals **14**, 446 (1987).

⁶ W. F. Müller and W. Schreyer, Eur. J. Mineral. **3**, 915 (1991).

⁷ J. Vicens and F. Delavignette, Phys. Stat. Sol. (a) **33**, 497 (1976). The authors argue that the low- T phase is likely monoclinic.

⁸ R. Sinclair and J. Dutkiewicz, Acta Metall. **25**, 235 (1977). The material studied is Mg₃Cd.

⁹ Y. Kitano, K. Kifune and Y. Komura, J. Phys. (Paris) **49**, C5-201 (1988); Y. Kitano and K. Kifune, Ultramicroscopy **39**, 279 (1991). The composition of the ‘‘MgCd alloy’’ is not specified.

¹⁰ C. Manolikas and S. Amelinckx, Phys. Stat. Sol. (a) **60**, 607 (1980).

¹¹ C. Manolikas and S. Amelinckx, Phys. Stat. Sol. (a) **61**, 179 (1980).

¹² E. K. H. Salje, Phys. Chem. Minerals **14**, 455 (1987).

¹³ A. C. E. Reid and R. J. Gooding, Physica A **239**, 1 (1997).

¹⁴ J. F. Blackburn and E. K. H. Salje, J. Phys.: Condens. Matter **11**, 4747 (1999).

¹⁵ J. F. Blackburn and E. K. H. Salje, Phys. Chem. Minerals **26**, 275 (1999).

¹⁶ Y. H. Wen, Y. Wang and L. Q. Chen, Acta Mater. **47**, 4375 (1999).

¹⁷ G. R. Barsch and J. A. Krumhansl, Phys. Rev. Lett. **53**, 1069 (1984).

¹⁸ S. H. Curnoe and A. E. Jacobs, cond-mat preprint 0004387.

¹⁹ A. E. Jacobs, Phys. Rev. B **31**, 5984 (1985).

²⁰ A. E. Jacobs, Phys. Rev. B **61**, 6587 (2000).

- ²¹ K. Fuchizaki and Y. Yamada, Phys. Rev. B **40**, 4740 (1989).
- ²² A. E. Jacobs, Phys. Rev. B **46**, 8080 (1992).
- ²³ A. Onuki, J. Phys. Soc. Jpn. **68**, 5 (1999).
- ²⁴ L. D. Landau and E. M. Lifshitz, *Theory of Elasticity*, (Pergamon Press, 1959).
- ²⁵ R. V. Kohn and S. Müller, Philos. Mag. A **66**, 697 (1992).
- ²⁶ W. C. Kerr, M. G. Killough, A. Saxena, P. J. Swart, and A. R. Bishop, Phase Transit. **69**, 247 (1999).
- ²⁷ S. R. Shenoy, T. Lookman, A. Saxena, and A. R. Bishop, Phys. Rev. B **60**, 12 537 (1999).

COLOUR FIGURES

FIG. 2. Samples of static configurations. The three different orthorhombic variants are represented as red, blue and green; the high-temperature phase is represented as black. Part (a) shows a very stiff system ($\zeta = 1000$) at low temperature ($\tau = -50$); the microstructure is dominated by nested stars and (1,3,5,3) zero-disclination nodes. Part (b) shows another very stiff system ($\zeta = 1000$), but at $\tau = 0.8$, just below the transition temperature ($\tau = 1$). The important features are the triangular and trapezoidal regions of trapped high- T phase and the (1,1,1,1,7) fan nodes.

FIG. 3. Snapshots of dynamical simulations at different times for identical starting conditions and different values of the stiffness parameter, at $\tau = -50$ (well below the transition temperature). Each frame has size 51.2×51.2 ; the colour scheme is as in Figure 2. Parts (a), (b) and (c), with $\zeta = 10, 100$ and 1000 respectively, show early-time structures ($t=0.255$) evolving from the perturbed high- T phase. The transformed region expands and then collides with images of itself because of the periodic boundary conditions; at later times the transformed phase occupies the whole frame. Part (d), a continuation of part (b) at time $t = 8.191$, shows several narrow domains or “streamers”. Parts (e) and (f) are continuations of part (c) at times $t = 0.511$ and $t = 16.383$ respectively. Part (e) shows transitory structures associated with stiff systems, namely bi-domain striations and star embryos. Part (f) is a fully relaxed configuration.

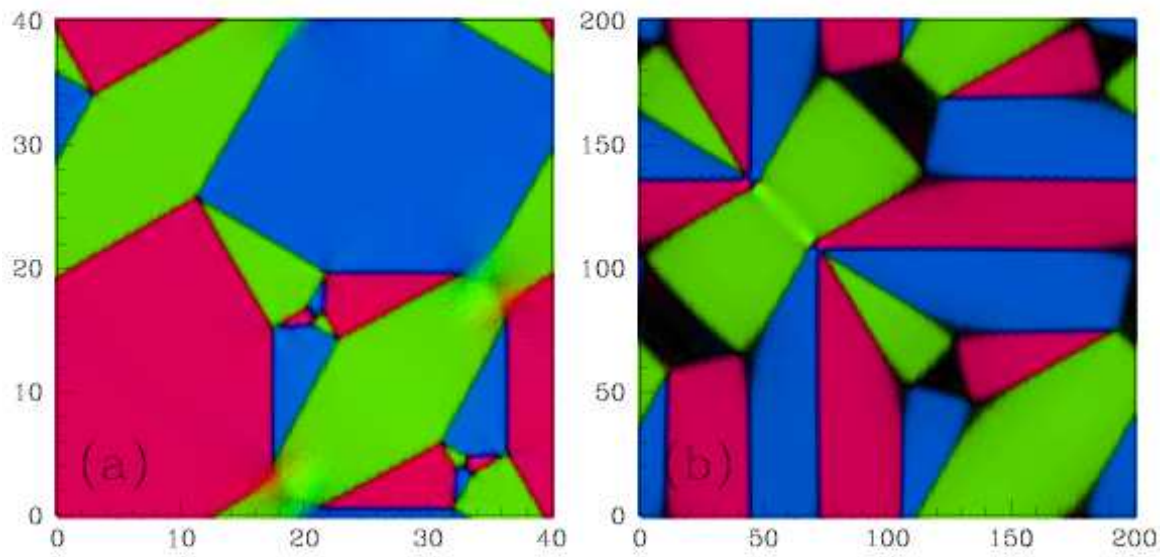


Figure 2

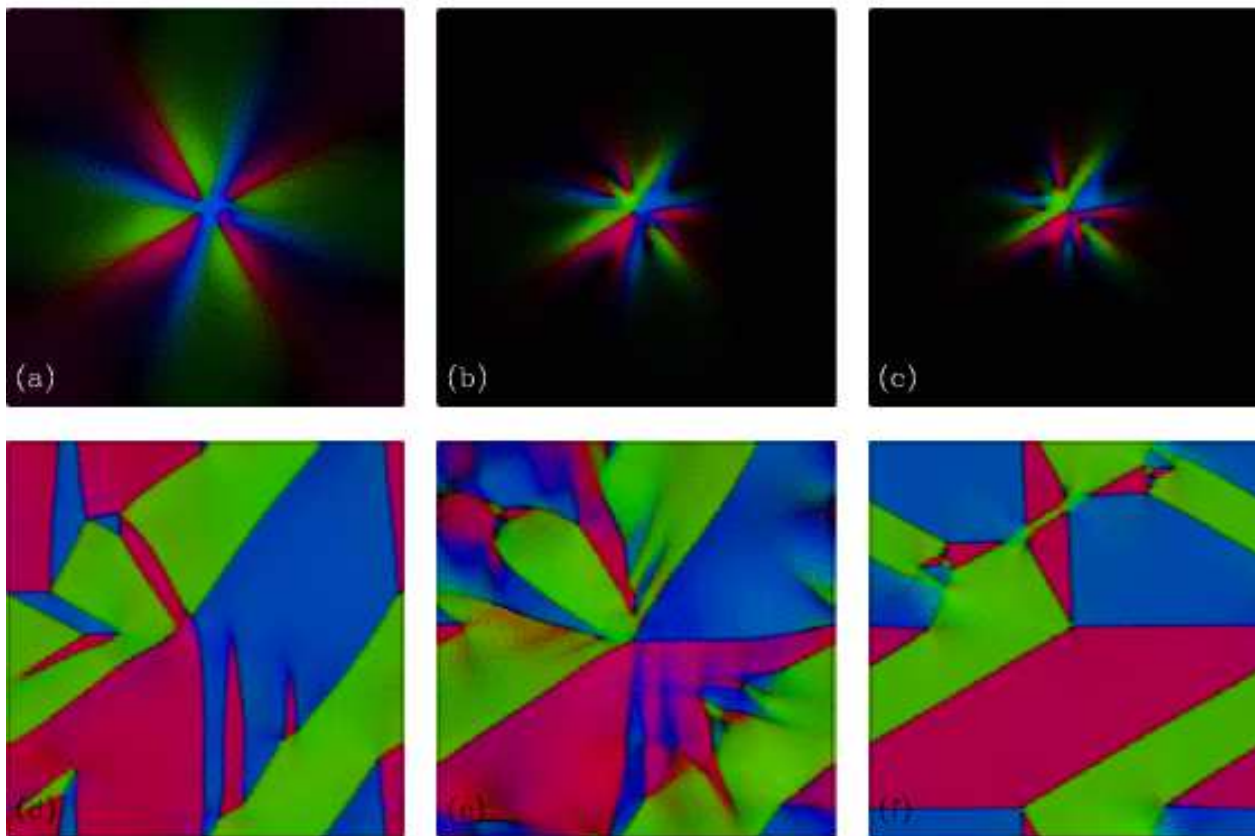


Figure 3